eprints@whiterose.ac.uk
https://eprints.whiterose.ac.uk/

Supplemental Materials

This supplemental information provides a detailed description of the datasets and methods used to calculate fault slip rates, including an assessment of uncertainties.

Probabilistic slip rate analysis

We developed a Monte Carlo simulation approach that characterizes uncertainties in geometrical measurements from subsurface data and combines them with uncertainties in our age constraints to produce slip rate probability distributions.

To determine relative timing and magnitude of fault slip, we rely on the paleo-fold geometries recorded by growth stratigraphy. Growth stratigraphy has been used in previous studies to characterize folding associated with blind-thrust faults, providing limits on fault geometry and slip rates (Suppe et al., 1992; Shaw and Suppe, 1996; Shaw and Shearer, 1999; Leon et al., 2009). We adopt the results of recent studies that show vertical relief of growth strata in fault-bend folds to be the best indicator of fault slip (Leon et al., 2007; Dolan et al., 2003; Leon et al., 2009; Benesh et al., 2007; Pratt et al., 2002). To measure the fold geometry above the LA segment, we used a collection of 43 oil industry seismic reflection profiles that image below ~300 m depth (Figure 1d). A shallow, high-frequency seismic reflection profile was acquired along Budlong Avenue in central LA across the shallowest portion of the forelimb observed in the industry seismic reflection data (Figure 1C). These data target the uppermost layers of the fold, which record the late Pleistocene to Holocene activity of the underlying fault. A weight drop source was used to image in the 100 – 700 m depth range (Pratt et al., 2002). Multiple impacts per shot point

were summed to suppress electrical and traffic noise. Processing techniques were as described in Pratt et al. (2002). The most recent activity on the LA segment was constrained by a series of eleven, 17 – 34 m deep continuously cored hollow-stem auger boreholes (Figure 1B), and a 175-m-deep borehole drilled into the forelimb of the structure.

To quantify deformation rates in the late Quaternary, sequence stratigraphic boundaries were interpreted across our seismic reflection data based on diagnostic reflection patterns and well-log correlations (Mitchum et al., 1977; Neal and Abreu, 2009). In the LA coastal plain, sea level changed during the Quaternary due to global ice age cycles (Ponti et al., 2007). During glacial periods, erosion and sediment bypass to the ocean occurred, producing unconformities. During the interglacial periods, when sea levels were high, sediment accumulated in the basin. These cycles of sea level change formed diagnostic coarsening and fining upwards sediment packages that reflect progradation and retrogradation of the shoreline. Ponti et al. (2007) used these principles along with over 300 well logs and 3D seismic reflection data to produce a sequence stratigraphic model in the Long Beach, California area for hydrologic and tectonic studies. This model was further developed by Ehman and Edwards (2014). We extended their sequence stratigraphic model across the LA basin to our study site using additional well logs and our industry seismic reflection data. We measured thickness change across these sequence boundaries to define fault activity in the late Quaternary. Erosion and sediment bypass create the potential for denudation of the paleo-folds we seek to measure, which may add additional, uncharacterized uncertainty to our slip rates.

Lithological correlations based on grain size and color define the fold geometry in our borehole profile (Figure 1b). The shallow sediments sampled in our study are most likely overbank or sheetflood deposits related to periodic flooding of the LA River. Based on the work of Leon et al. (2007), we recognize that large slip events on the PHT blind-thrust fault formed fold scarps at the surface, as were observed after the 1999, M_w 7.6, Chi-Chi earthquake (Chen et al., 2007). Subsequent floods buried these scarps, forming growth stratigraphy. Our borehole profile contains a discontinuous, organic-rich soil that buttresses the fold and overlies a continuous clay and silt layer (Figure 1b). We interpret the organic-rich soil as having formed due to ponding at the base of a paleo-fold scarp that would have developed after deposition of the continuous clay and silt layer. We refer to this surface as top clay and use it to constrain the most recent deformation on the LA segment.

Velocity model uncertainties

The depths of reflectors in our seismic reflection data are functions of the average compressional-wave velocities $\overline{V}_p$ from the seismic source at the surface to the impedance contrasts at depth that produced them. These in turn are functions of the interval velocities V_i of the overlying materials (sediments and fluids) the waves passed through: $\overline{V}_p = \sum_{i=1}^{n} V_i t_i / \sum_{i=1}^{n} t_i$, where t_i is the one-way time for a compressional wave to travel across depth interval i. Stacking velocities from seismic reflection profiles are often used to estimate $\overline{V}_p$, but can have inaccuracies of 10% or more, particularly at shallow depths where velocities increase rapidly and the straight-raypath approximation used in common-midpoint velocity analyses does not hold. More accurate velocity determinations from the shallow reflection data, such as pre-stack migration methods, are difficult to implement

because of the relatively low signal-to-noise ratio and limited offset range after muting the surface waves and refracted arrivals.

Since we do not know the precise velocity structure, we instead determine the range of $\overline{V_p}$ by performing simulations that vary the magnitude and ordering of V_i. We accomplish this by developing an autoregressive (AR) statistical model based on interval-transit-time compressional-wave velocities (V_{ITT}) from a nearby industry well that we characterize relative to the Southern California Earthquake Center Community Velocity Model v11.9 with near-surface geotechnical layer (CVMH) (Suess and Shaw, 2003; Plesch et al., 2007; Shaw et al., 2015). The CVMH data are extracted at the center of each model grid cell, yielding 8 vertical velocity profiles at 250 m spacing across our study area (Data Repository Figure 2). The V_{ITT} data is from the Union-Standard La Tijera E.H. 1 well (API: 03700792), which is approximately 2.5 km east of our study site and likely contains similar lithologies. Velocities are measured at 0.15 m (6 in.) intervals and display positive autocorrelation, with successive observations persisting above and below the mean, suggesting an autoregressive process (Data Repository Figure 3). We perform AR modeling and validation using the ARfit analysis suite of Schneider and Neumaier (2001) and Neumaier and Schneider (2001), which uses a stepwise least squares algorithm to determine the parameters and model order that optimize Schwarz's Bayesian Criterion. The AR model assumes zero mean and normally distributed, temporally uncorrelated noise (residuals about the mean). The V_{ITT} data have a skewed distribution and non-zero mean (Data Repository Figure 3), so we perform a log transformation to improve normality and detrend the data by the log of its mean to get the velocity noise V_n we seek to characterize:

$V_n = \ln V_{ITT} - \ln \overline{V_{ITT}}$. Our best-fit model is: $V_d = \phi_1 V_{d-1} + \phi_2 V_{d-2} + \phi_3 V_{d-3} + \varepsilon_d$ where $\phi_1 = 1.2 \pm 0.035$, $\phi_2 = -0.066 \pm 0.055$, $\phi_3 = -0.14 \pm 0.035$, and variance $Var = 3.2 \times 10^{-4}$ for the noise vector ε_d ($\pm$ ranges denote 95% confidence intervals). We demonstrate that our model satisfies the correlation conditions using the modified Li-Mcleod portmanteau test, which yields a significance level of 0.18, indicating that the noise is uncorrelated at a 95% confidence level (Schneider and Neumaier, 2001; Neumaier and Scneider, 2001).

We use a Monte Carlo approach to simulate average velocities for depth conversion by adding iterations of AR noise to the CVMH interval velocities, and then calculating the resulting averages. For a single iteration i, the simulated interval velocity is characterized as $V_{sim_i} = e^{V_{d_i} + \ln \overline{V_{ITT}}} - \overline{V_{CVMH}} + V_{CVMH}$, where $e^{V_{d_i} + \ln \overline{V_{ITT}}}$ is the back-transformed simulation output, $\overline{V_{CVMH}}$ is the mean of the CVMH interval velocities at the position of the La Tijera well that shifts the simulations to their correct average position relative to the CVMH (Data Repository Figure 3), and V_{CVMH} are the CVMH interval velocities at our study area. We initialize the simulations with zero mean values and discard the first 1000 points. For each simulation, we calculate average velocities and corresponding travel times, and then interpolate the average velocities onto our time interpretations. A comparison of simulated average velocities to the CVMH at the La Tijera well location is shown in Data Repository Figure 4. The variance in average velocity decreases with depth as the number of sampled interval velocities above increases. We use the interpolated average velocities to depth-convert our interpretations of the sequence boundaries.

Seismic resolution uncertainties

The sequence boundaries used to define fold geometries in the Pleistocene may contain subtle unconformities and thin beds that are beyond the resolvable limit of our seismic reflection data due to attenuation of high frequencies at depth. We must therefore also consider the impact of resolution uncertainty on our results. Based on empirical $\pm\frac{1}{2}\lambda$ resolution limits from synthetic seismic simulations of sequence geometries (Vail et al., 1977), we conservatively bracketed our interpretations of the crest and trough about the fold using $\pm\frac{1}{2}\lambda$ uniform distributions. To do this, we first estimated the dominant period $\hat{\tau}_i$ along each interpreted sequence boundary as the time difference to the adjacent, underlying reflector, measured normal to the sequence boundary to account for folding, and halved to convert to one-way time. We then extracted the simulated interval velocities within $\pm\frac{1}{2}\hat{\tau}_i$ of the sequence boundary one-way time and averaged them to estimate the velocity $V_{\tau\,ave_i}$ within the resolution uncertainty region. Using this, we calculated the corresponding wavelength in meters: $\hat{\lambda}_i = V_{\tau\,ave_i}\hat{\tau}_i$. To simulate potential sequence boundary positions within the resolution range, we sampled the $\pm\frac{1}{2}\hat{\lambda}_i$ resolution distribution separately for the trough and crest for each iteration i, and shifted each by the sampled value. To correspondingly shift the data across the fold, we calculated the slope of the lines defined by the crest and trough endpoints before and after adding the resolution uncertainty. We then shifted the fold data by the vertical difference between the two lines evaluated at each horizontal position. Data Repository Figure 5 shows an example simulated fold geometry.

Uplift, fault dip, and slip calculations

To estimate uplift U_i, we used the difference between average stratal thickness on the crest and trough of the fold, calculated at 15 m increments normal to the overlying surfaces to account for regional dip (Data Repository Figure 5). To account for any potential thickness changes across the fold due to differential compaction, we used the exponential porosity-depth relations of Athy (1930) to estimate the decompacted average trough and crest thicknesses at the time of deposition. In the Athy relations, the change in porosity ϕ with depth z is given by $\phi = \phi_0 e^{-cz}$, where ϕ_0 is the initial porosity at the surface and c is an empirically determined compaction coefficient. We do not have direct measurements of porosity near our site, so we instead sample from a range of initial porosities ϕ_{0_i} (0.375 – 0.8) and constants c_i (0.25 – 0.9) for each iteration i, consistent with the sands and silts present at our site (Sclater and Christie, 1980; Bahr et al., 2001; Allen and Allen, 2005). The decompacted thickness of a layer $\Delta z_i{'}$ is given by:

$$\Delta z_i{'} = z_{b_i} - z_{t_i} - \frac{\phi_{0_i}}{c_i}(e^{-c_i z_{t_i}} - e^{-c_i z_{b_i}}) + \frac{\phi_{0_i}}{c_i}\left(e^{-c_i z{'}_{t_i}} - e^{-c_i z{'}_{b_i}}\right)$$

where $z{'}_{b_i}$ and $z{'}_{t_i}$ are the decompacted bottom and top of the layer and z_{b_i} and z_{t_i} are the present-day, compacted bottom and top of the layer (Allen and Allen, 2005). These equations are solved by numerical iteration.

Since the growth stratal geometries are consistent with fault-bend folding theory, we used the fault-bend fold kinematic model (Suppe, 1983) to calculate fault dip θ_i : $\theta_i = \tan^{-1}(\sin 2\gamma_i/(1 + 2\cos^2 \gamma_i))$, where γ_i is the angle of the axial trace and the fault is assumed to shallow to a bedding parallel detachment, similar to the geometry proposed for

the Santa Fe Springs segment. The axial trace is defined as the angle bisector between folded and unfolded strata. We calculated dip using a first-order least-squares fit along the trough and steepest portion of the fold from which we calculated axial trace angles (Data Repository Figure 5). From the results of Benesh et al. (2007), the sequence boundary with the steepest fold dip should be used for fault dip calculation. We therefore use the steepest dipping, central portion of the Bent Spring sequence boundary to calculate fault dip. Due to our study's urban setting, our seismic reflection profile was not acquired parallel to dip, so we randomly sampled a uniform distribution between N55°W and N65°W strike for apparent dip corrections. The fault dips θ_i derived from these measurements were then used to calculate fault slip S_i as $S_i = U_i/\sin\theta_i$. Uplift and fault dip were calculated from the same simulated geometry to ensuring proper correlation between measurements.

We note that alternative fault-related fold kinematics would raise the possibility of other relations between uplift and slip. Specifically, some classes of fault-propagation folds (e.g., Suppe and Medwedeff, 1990) indicate a fixed but higher ratio of uplift to fault slip than do fault-bend folds, while break-through fault-propagation folds and detachment folds suggest that uplift rates may decelerate over time with constant slip rate (e.g., Rockwell et al., 1988; Hubbard et al., 2014). However, neither fault-propagation nor detachment folds are consistent with the growth structure at our site, which is a discrete feature localized above the anticlinal axis of the structure (Suppe, 1992; Pratt et al., 2002; Shaw et al., 2002; Dolan et al., 2003). Moreover, those models imply that the ratio of uplift to slip rate would decreases through time (see Hubbard et al., 2014). This would enhance, rather than diminish, the calculated increase at our site.

Age control and uncertainties

Age control was provided by accelerator mass spectrometer radiocarbon dating (^{14}C), infrared stimulated luminescence dating (IRSL), and sequence boundaries matched to δ^{18}O curves. Radiocarbon ages were calibrated with Oxcal v.4.2.4 Reimer et al., 2013) and are shown with $\pm 2\sigma$ bounds on Figure 1b. Detailed results are shown in Data Repository Table 1a. In our simulations, we randomly sampled an empirical distribution that brackets the burial age of the top clay using the Oxcal probability density functions for samples from well 8 and well 5 (Figure 1B). The empirical distribution was created by combining the cumulative density function of the well 8 sample with the reflection of the cumulative density function of the older well 5 sample, and assigning uniform probability between the two (Data Repository Figure 6).

To define deposition and deformation rates further into the past, light-protected samples were obtained for single grain K-feldspar IRSL dating at borehole D1 (Figure 1B, 1C). We used hollow-stem auger drilling to collect samples down to ~40 m depth and mud-rotary drilling to collect samples down to ~135 m depth. For the hollow-stem auger drill rig, we used a split-spoon sampling tool fitted with a stainless steel liner that was driven into the ground in front of the drill bit, ensuring an *in situ* and uncontaminated sample (Data Repository Figure 7A). The liner shielded the sediments from light-exposure when the sample was recovered at the surface. Once removed from the split-spoon sampler, the sample liner was capped and placed in a light-proof bag. For the mud-rotary drill rig, we also used stainless steel liners inside a split-spoon sampler. The sampling tool sat in front

of the drill bit to avoid collecting sediment altered by the drilling process (Data Repository Figure 7B). We collected luminescence samples from only well-compacted sediment (based on resistance to drilling), minimizing the risk that drilling mud would infiltrate pore space and contaminate the sample with younger or light-exposed sediment grains.

Single grain K-feldspar post-IR IRSL (Infra-Red Stimulated Luminescence) determinations of six samples were used to provide age control for the upper 140m of the stratigraphic sequence (Data Repository Tables 1b, 2). This dating approach was developed specifically for application to fault slip-rate and paleoseismology contexts, and has been assessed at a number of similar sites in California and elsewhere (Rhodes, 2015).

Sediment samples were extracted from steel core tubes under controlled laboratory lighting conditions at UCLA, avoiding material that might have been exposed to daylight during coring operations. After suspension separation of the silty component, samples were wet sieved and the 180 - 212μm fraction retained. After dilute HCl treatment and drying, the fraction <2.58 g.cm^{-3} was separated using lithium metatungstate (LMT) for each sample, and these fractions were subsequently treated with dilute (10%) HF for 10 mins. to etch grain surfaces.

Measurements were made at UCLA using a Risø automated TL-DA-20 luminescence reader fitted with a single grain dual laser system. A single aliquot regenerative-dose (SAR) protocol modified from that of Buylaert et al. (2009) for application to single grains. Measurement details are provided in Data Repository Table 1b. The signal used to estimate

age was the background- subtracted initial IRSL at 225°C (the post-IR IRSL; step 4 in Data Repository Table 2) corrected for sensitivity changes using the sensitivity measurement at 225°C (step 8 in Data Repository Table 2). The sensitivity-corrected regenerative-dose signals were fitted with an exponential (or exponential plus linear) function, used to estimate the equivalent dose (D_e) and 1-sigma uncertainty values for each grain. After the measurement of the equivalent dose, fading measurements were performed for each measured grain.

Data Repository Figure 8 shows the fading-corrected apparent ages for each grain from the six post-IR IRSL samples in stratigraphic order, with the uppermost sample (J0243) at the top. Results are plotted in rank order of signal sensitivity of the post-IR IRSL to a fixed test dose within the SAR dating protocol, with the most sensitive grain at position 1, decreasing to the least sensitive grain plotted. These plots show the apparent age and 1-sigma uncertainty values for all grains that provided an equivalent dose estimate; grains with insensitive IRSL responses display no growth or large uncertainties on the D_e values, and consequently are not shown. All samples provide D_e estimates for many grains (between 70 and 230 results), corresponding to 35 to 80% yield from the 200 or 400 (J0246 only) grains measured.

The sample responses fall into two broad groups. The first type of behavior is characterized by a shared, uniform minimum D_e value, irrespective of grain sensitivity. The uppermost three samples display this behavior. For these samples, a shared minimum equivalent dose value was determined using the procedure described by Rhodes (2015) assuming an over-

dispersion value of 15% to account for variations in single grain beta dose rate, and differences in response to the dating protocol applied. This procedure is conceptually similar to the minimum age model (MAM) of Galbraith et al. (1998) but involves fewer assumptions about the form of the overall dose distribution, is insensitive in applicability to sample size (i.e. the number of results available), and treats dose values as either included or excluded, rather than fractionally included as is the case for the MAM. The comparisons of single grain post-IR IRSL with independent age performed by Rhodes (2015) were made using this approach. In Data Repository Figure 8, grains included in this way are shown by solid symbols.

The second behavior witnessed in these samples is clearly displayed by samples J0268 and J0247 from lower in the stratigraphy. Rhodes (2015) terms this behavior "declining base" as the plot of D_e (or as in this case, apparent age) vs. rank order sensitivity shows a systematically declining minimum value. Samples from known-age locations in California that displayed this behavior e.g. late Pleistocene samples with good radiocarbon control from Rialto, CA) provided age estimates in agreement with independent control when the minimum value of only the brightest (most sensitive) grains are included in the age calculations. The criterion for including grains depends on the rate of decline as function of rank order sensitivity; grains above the point where this trend of the minimum D_e value declines by the value of the assumed over-dispersion (in this case 15%) from its initial value for the most sensitive grain are included, and those with rank order sensitivity below this point are excluded, as observed for samples J0268 and J0247 in Data Repository Figure

8. The results for sample J0246 had lower precision on average, so that all grains were included in the age estimate.

There was some degree of variation in the measured mean fading values for different samples, probably arising from subtle longer-term sensitivity changes. An approach that incorporated the measured fading values and the independent stratigraphic and age control data (for the highest sample only) was used. Dose rates were based on ICP-MS values for U and Th, and ICP-OES for K. Corrections for internal beta dose rate from K, and attenuation of external radiation by grain size and water content were performed, and the small cosmic radiation dose rate contribution calculated as in Rhodes et al. (2010). The fading-corrected age estimates are provided in Data Repository Table 1b, and shown by the dashed lines in Data Repository Figure 8.

We used $\delta^{18}O$ marine isotope stages (MIS) to define sequence boundary ages, based on the sequence stratigraphic model of Ponti et al. (2007). The temporal relationship between sequence boundaries and changes in base level remains a topic of considerable research (Törnqvist et al., 2003). As such, we conservatively bracket the ages of our sequence boundaries between $\delta^{18}O$ minima (corresponding to relative sea level highstands) and maxima (corresponding to relative sea level lowstands), encompassing the range of theorized sequence boundary age relationships. Independent age constraints within the sequences, including thermoluminescence ages, volcanic tephra, paleontological studies, and paleomagnetic susceptibility, support the age framework (Ponti et al., 2007; McDougall et al., 2012). Using the MIS stages of Basinot et al. (1994), we placed age of the Harbor

sequence boundary between MIS 7.1 and 6.2 (194 – 133 ka), the Bent Spring sequence

boundary between MIS 9.3 and 8.2 (328 – 248 ka), and the Upper Wilmington sequence

boundary between MIS 13.1 and 12.2 (474 – 434 ka). We sampled uniform distributions

across these ranges in our simulations (Data Repository Figure 6).

Slip rate calculation

To produce slip rate probability distributions SR_i, we divided our slip estimates between

stratigraphic markers S_i by the changes in time Δt_i between random samples from the

corresponding age distributions: $SR_i = S_i/\Delta t_i$. We performed 50,000 iterations of our

Monte Carlo analysis. After 10,000 iterations, slip rate means varied by less than 2.5% of

the full simulation, but we performed additional iterations to better define the distributions

and ensure adequate coverage of less frequent parameter combinations.

Supplemental Figures
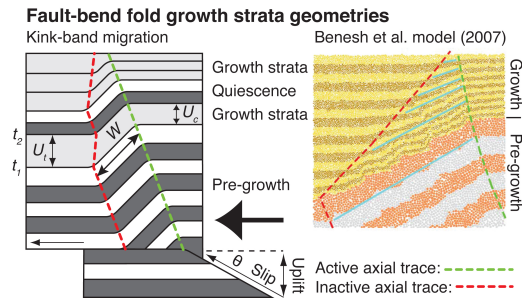
Data Repository Figure 1. Kinematic model of a fault-bend fold with growth stratigraphy showing migration of the synclinal, inactive axial trace and fold growth by kink-band migration (Suppe et al., 1992). The width of the fold limb W decreases towards the surface as younger strata have undergone less uplift and translation. The results of Benesh et al. (2007) highlight the shallowing dips (limb-rotation) and kink-band migration found from modeling the behavior of unconsolidated sediment as would be expected for growth stratigraphy. Assuming the change in thickness $U = U_t - U_c$ is equal to uplift, slip is then given by $S = U/\sin\theta$. If ages at the base t_1 and top t_2 are known, the slip rate SR over that time interval can be calculated as $SR = S/\varDelta t$, where $\varDelta t = t_1 - t_2$.
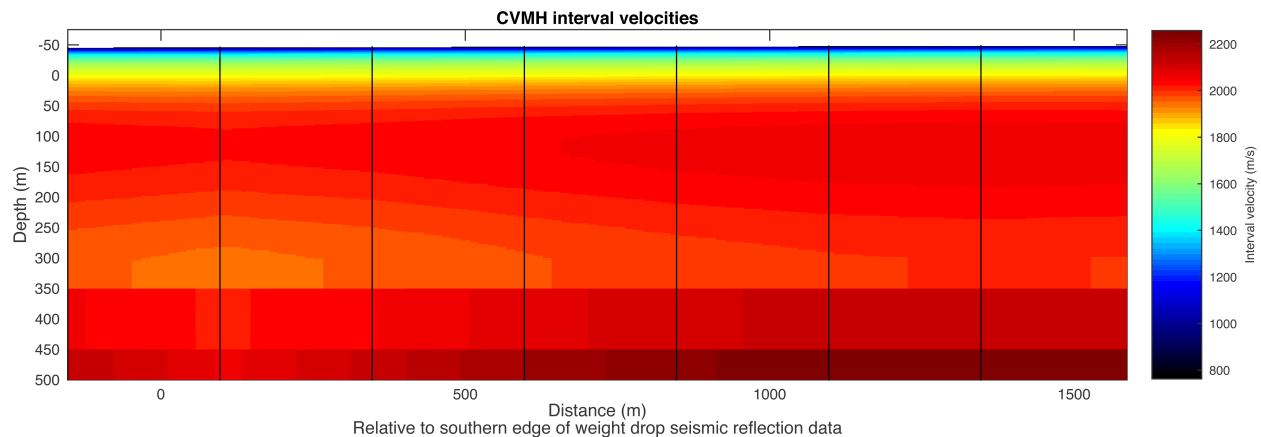
Data Repository Figure 2. Interval velocities along our weight drop seismic reflection profile from the Southern California Earthquake Center Community Velocity Model v11.9 with near-surface geotechnical layer (CVMH). Vertical lines show the centers of each CVMH grid cell. For this plot, we interpolate interval velocities from the CVMH onto a 15 m horizontal by 1 m vertical grid.
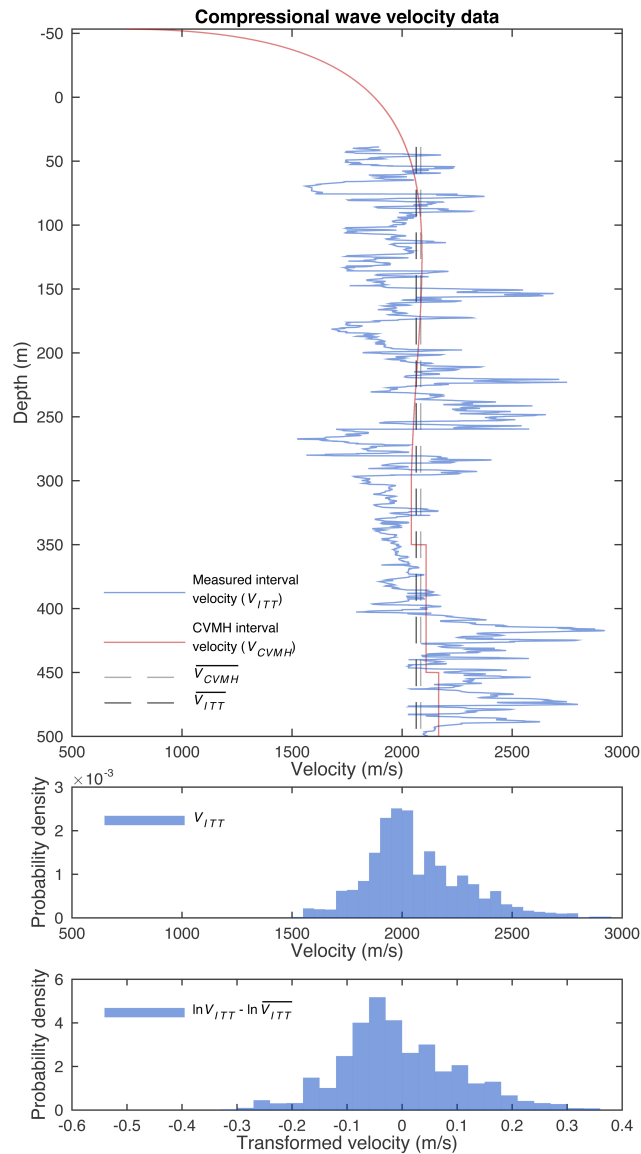
Data Repository Figure 3. Interval velocity V_{ITT} measurements from the La Tijera well with the CVMH interval velocities V_{CVMH} also shown. Over the well depth range, the average

velocities for each are very similar, with the observed data being slower by 20 m/s. A

normalized histogram of the raw V_{ITT} is shown in the middle figure. It has a slightly

lognormal distribution. We use a log transformation, as shown in the lower figure, to

improve normality and better satisfy the requirements for Gaussian noise in the AR

modeling approach.
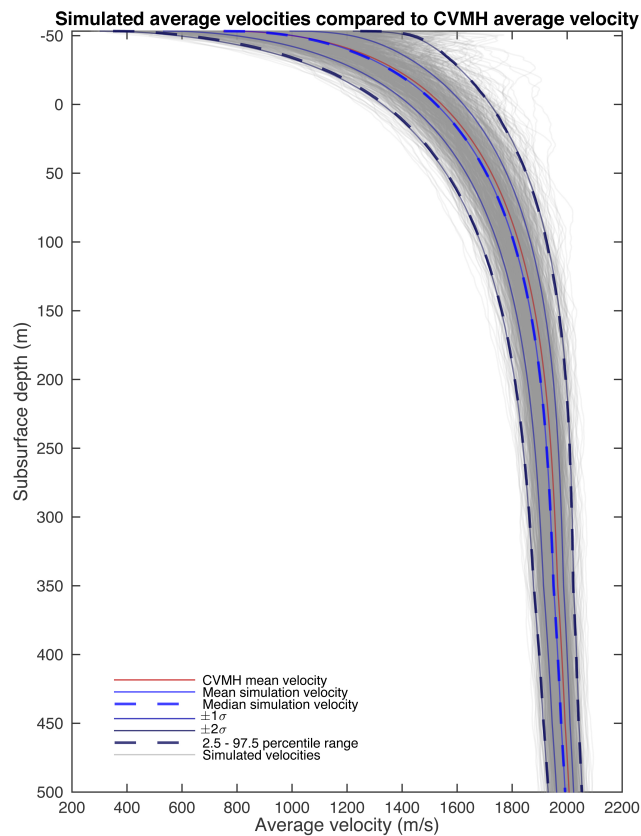
Data Repository Figure 4. Average velocities from our simulations compared to the CVMH

average velocity at the La Tijera well location. Average velocities from the first 500

simulations are plotted in semi-transparent grey to give a sense of their density and range.

All other statistics are based on data from 50,000 simulations. The average velocity

variance decreases with depth because we are averaging over an increasing number of

interval velocity samples with the same underlying distribution.
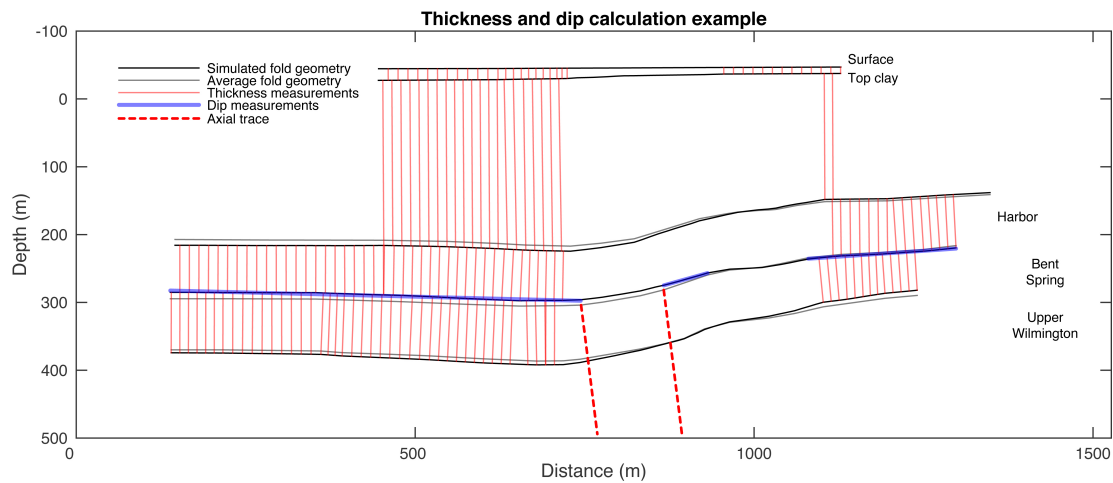
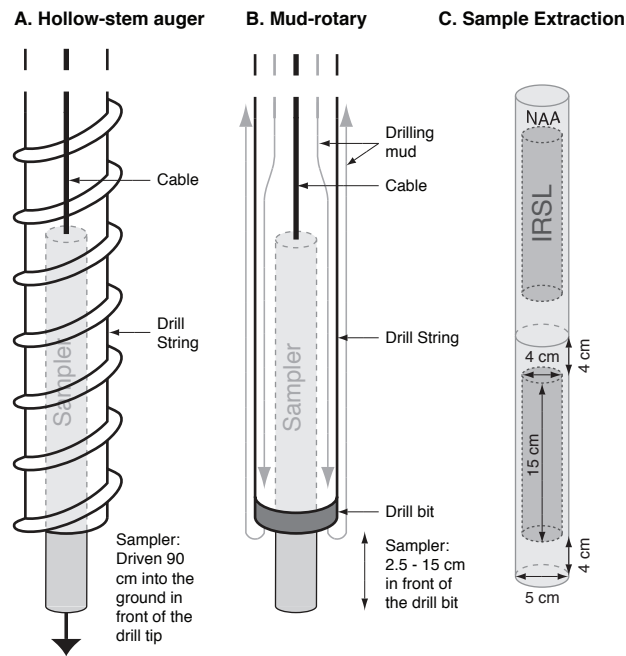**Data Repository Figure 5.** Thickness and dip measurement example. The position of the

top clay does not vary as it is defined lithologically by our boreholes.
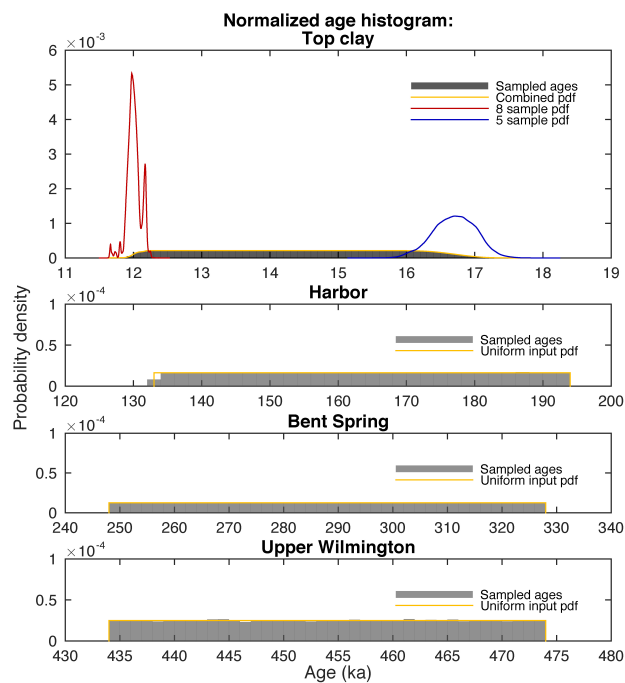
Data Repository Figure 6. Probability density normalized age distributions. The

combined probability distribution for top clay was produced by combining the cumulative

distribution function for the ^{14}C sample from well 8 with the reflection of the cumulative

distribution function for the ^{14}C sample from well 5. We assume uniform probability in

between. We use uniform distributions for the sequence boundary ages.

A. Hollow-stem auger **B. Mud-rotary** **C. Sample Extraction**

Cable

Drill String

Sampler: Driven 90 cm into the ground in front of the drill tip

Drilling mud

Cable

Drill String

Drill bit

Sampler: 2.5 - 15 cm in front of the drill bit

NAA

IRSL

4 cm

15 cm

4 cm

4 cm

5 cm

Data Repository Figure 7. Schematic diagram of hollow-stem auger sampling technique. b.

Schematic diagram of mud-rotary drill rig sampling technique used for IRSL dating. c.

Diagram of sample extraction from the stainless steel liner in the laboratory. The portion

labeled NAA was used for ionizing dose-rate determination and the portion labeled IRSL

was used for luminescence measurement.
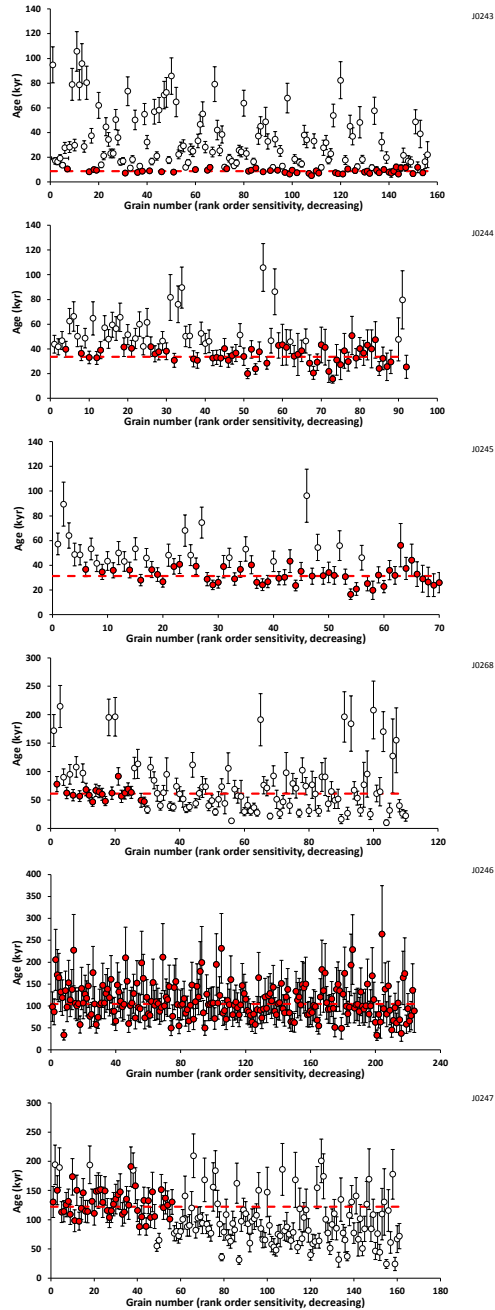
Data Repository Figure 8. Single grain K-feldspar post-IR IRSL results for six sediment samples from the Puente Hills core. Data are present as apparent age for each grain that provided an equivalent dose result for each sample, with its associated 1-sigma uncertainty, in stratigraphic order with the youngest sample at the top of the figure. Apparent age data are presented in rank order of signal sensitivity of the post-IR IRSL to a fixed test dose

within the SAR dating protocol, with the most sensitive grain at position 1, decreasing to the least sensitive grain plotted. A variety of different sample responses is observed, corresponding to variations in K-feldspar behavior likely associated with changes in sediment sources deposited over this time period (last interglacial to Holocene). Solid symbols show results for grains included in the combined age estimate for that sample, open symbols show excluded grains. See text for further details.
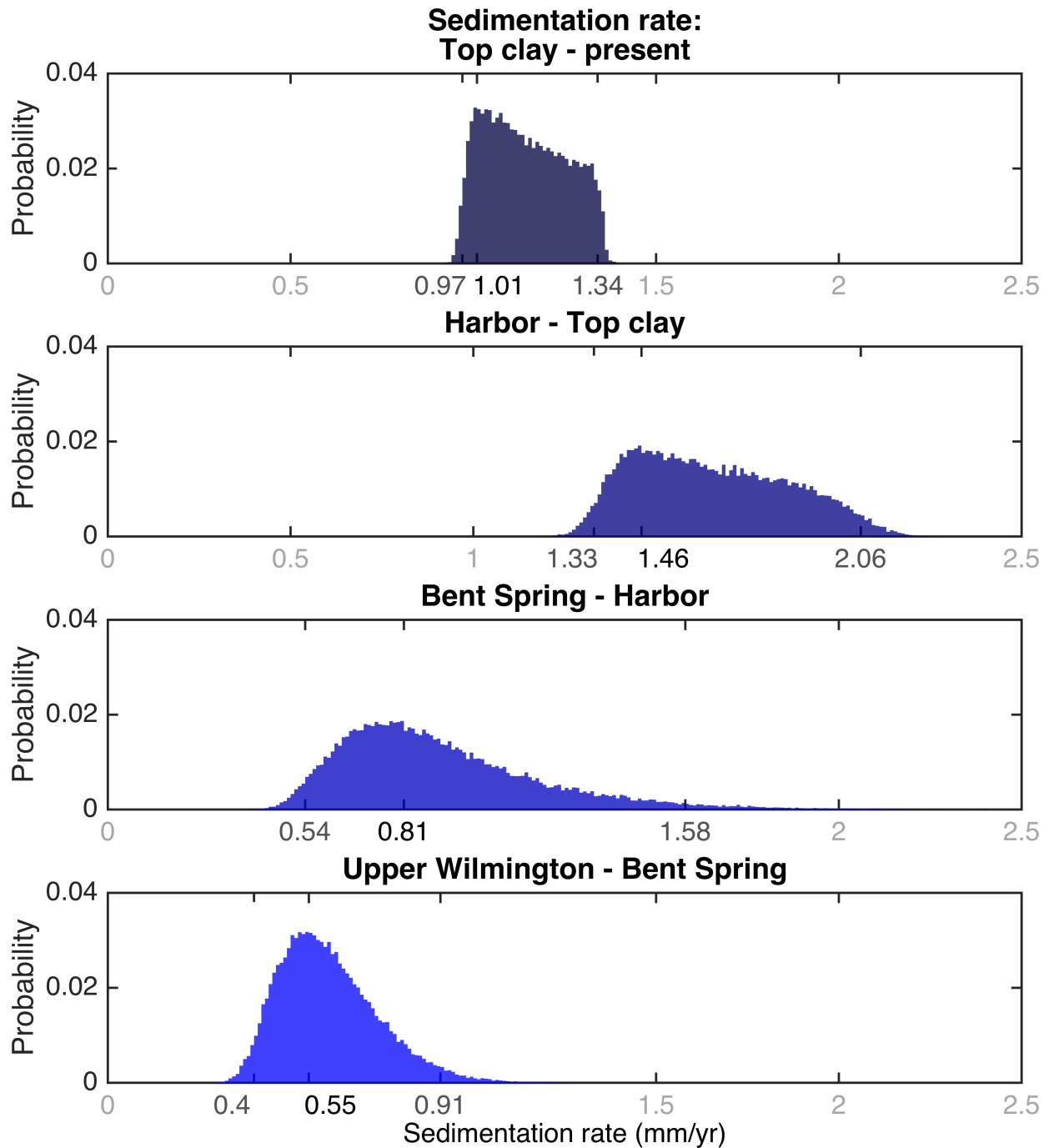
Data Repository Figure 9. Probability normalized histograms of sedimentation rates. The 2.5 – 97.5 percentile ranges are shown, along with median values for symmetric distributions and modal values for skewed distributions. Bin size is 0.1 mm/yr.
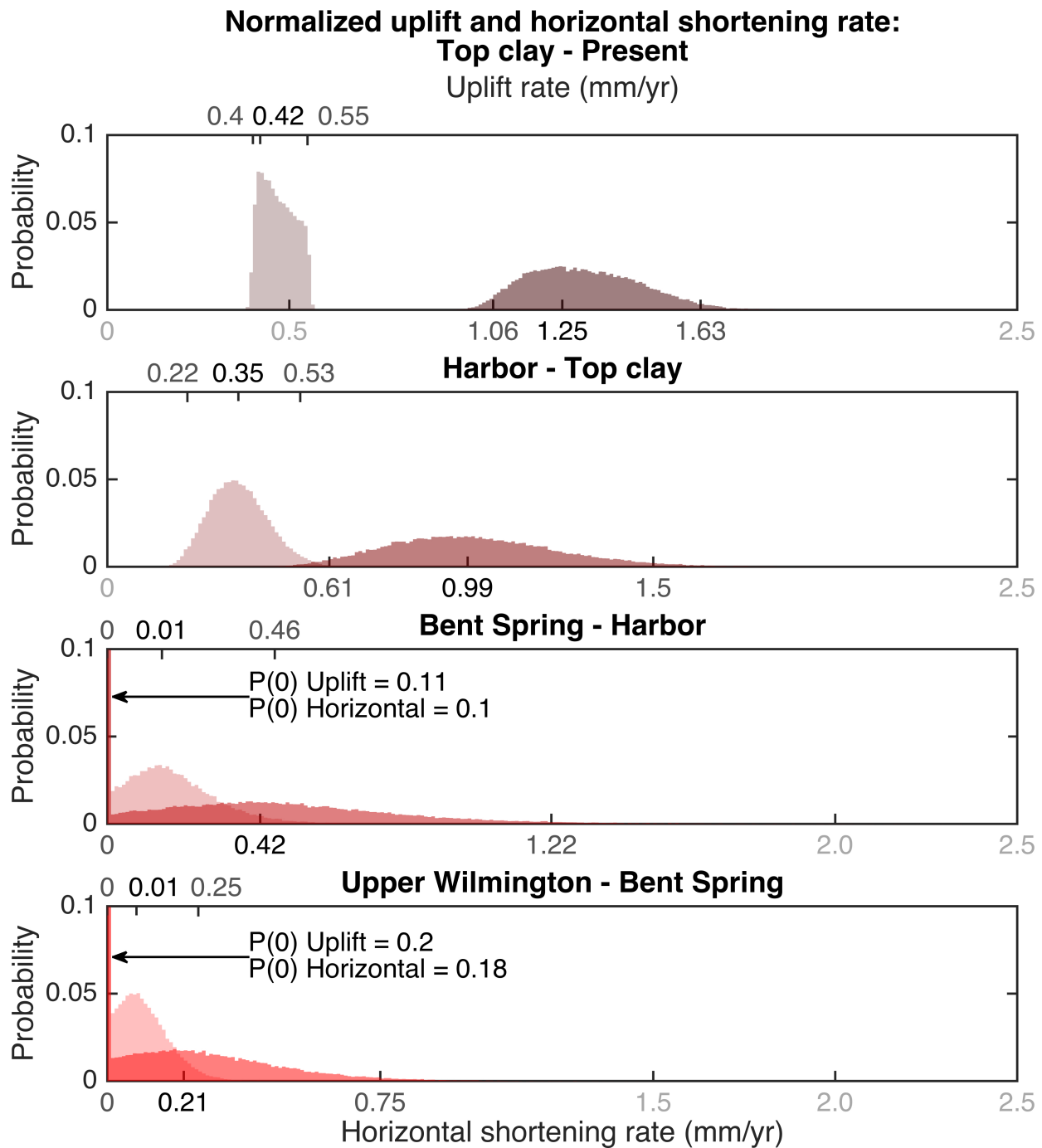
Data Repository Figure 10. Probability normalized histograms of uplift and horizontal shortening rates. The 2.5 – 97.5 percentile ranges for horizontal shortening rates (along the bottom axis) and for uplift rates (along the top axis), with median values for symmetric distributions and modal values for skewed distributions. Bin size is 0.1 mm/yr.

a. Radiocarbon ages and sample details

Borehole	Sample type	Depth (m)	^{14}C Age BP	^{13}C	Calibrated age BP (1950) 68.2% Probability	95.4% Probability
D1	Small charcoal	7.47	6960 ± 100	-25	7923 – 7902 (6.7%) 7866 – 7692 (61.5%)	7966 – 7617 (95.4%)
D1	Medium charcoal	8.69	7390 ± 170	-25	8360 – 8043 (68.2%)	8544 – 7928 (94.7%) 7895 – 7874 (0.7%)
10	Bulk soil	15.93	9465 ± 35	-25	10752 – 10659 (65.9%) 10614 – 10610 (2.3%)	11060 – 11036 (2.3%) 10996 – 10978 (1.6%) 10788 – 10584 (91.5%)
2	Bulk soil	15.52	9980 ± 40	-25	11602 – 11551 (14.7%) 11494 – 11432 (16.5%) 11412 – 11309 (37%)	11620 – 11265 (95.4%)
8	Bulk soil	16.16	10265 ± 40	-25	12114 – 11957 (64.9%) 11862 – 11849 (3.3%)	12226 – 12217 (0.4%) 12166 – 11819 (95%)
5	Bulk soil	11.28	13780 ± 210	-25	16980 – 16348 (68.2%)	17326 – 16090 (95.4%)

b. IRSL ages and sample details

Borehole	Drilling technique	Field Code	Lab code	Depth (m)	Equivalent dose ± 1σ uncertainty (Gy)	Total dose rate ± 1σ uncertainty (mGy/yr)	Age ± 1σ uncertainty (ka)
D1	Hollow-stem	HS PHD1 30.5'-32'	J0243	9.4	30.9 ± 1.0	3.55 ± 0.18	8.70 ± 0.53
D1	Hollow-stem	HS PHD1 65'-66.5'	J0244	20.0	117 ± 4	3.47 ± 0.24	33.7 ± 2.6
D1	Hollow-stem	HS PHD1 75'-76.5'	J0245	23.0	107 ± 4	3.42 ± 0.22	31.4 ± 2.3
D1	Hollow-stem	HS PHD1 131.5'-133'	J0228	40.2	192 ± 8	3.14 ± 0.21	61.1 ± 4.9
D1	Mud-rotary	MR PHD2 395'-396.5'	J0246	120.5	317 ± 10	3.03 ± 0.20	105 ± 8
D1	Mud-rotary	MR PHD2 444.5'-446'	J0247	135.5	403 ± 13	3.23 ± 0.20	125 ± 9

c. Sedimentation rate statistics (mm/yr)

	2.5%	Mean	Median	Mode	97.5%	σ	CVMH
Top clay – Present	0.97	1.14	1.13	1.01	1.34	0.11	1.13
Harbor – Top clay	1.33	1.65	1.63	1.46	2.06	0.21	1.67
Bent Spring – Harbor	0.54	0.91	0.85	0.81	1.58	0.27	0.87
Upper Wilmington – Bent Spring	0.4	0.6	0.59	0.55	0.91	0.13	0.6

d. Slip rate statistics (mm/yr)

	2.5%	Mean	Median	Mode	97.5%	σ	CVMH
Top clay – Present	1.13	1.4	1.38	1.33	1.73	0.16	1.36
Harbor – Top clay	0.65	1.07	1.05	1.01	1.6	0.24	1.06
Bent Spring – Harbor	0	0.48	0.45	0.01	1.3	0.36	0.45
Upper Wilmington – Bent Spring	0	0.26	0.22	0.01	0.8	0.23	0.24

e. Uplift rate statistics (mm/yr)

	2.5%	Mean	Median	Mode	97.5%	σ	CVMH
Top clay – Present	0.4	0.47	0.47	0.42	0.55	0.05	0.47
Harbor – Top Clay	0.22	0.36	0.36	0.35	0.53	0.08	0.36
Bent Spring – Harbor	0	0.17	0.15	0.01	0.46	0.13	0.15
Upper Wilmington – Bent Spring	0	0.09	0.08	0.01	0.25	0.07	0.08

f. Horizontal shortening rate statistics (mm/yr)

	2.5%	Mean	Median	Mode	97.5%	σ	CVMH
Top clay – Present	1.06	1.31	1.3	1.25	1.63	0.15	1.28
Harbor – Top Clay	0.61	1.01	0.99	0.95	1.5	0.23	0.99
Bent Spring – Harbor	0	0.45	0.42	0.01	1.22	0.34	0.42
Upper Wilmington – Bent Spring	0	0.24	0.21	0.01	0.75	0.22	0.22

g. Fault dip statistics (°)

	2.5%	Mean	Median	Mode	97.5%	σ	CVMH
Fault Dip (°)	17.14	19.78	19.84	19.95	22.15	1.29	20.03

Data Repository Table 1. Data tables from age determinations (a, b) and fault slip and geometry simulations (c – g). Table b. shows details for the combined single grain post-IR IRSL data used in the depositional age model. For tables c – g, the 2.5% and 97.5% headings correspond to the 2.5 – 97.5 percentile ranges. Modes are calculated from histograms with 0.1 mm/yr bins for rate estimates, and 0.1° bins for dip estimates. CVMH values correspond to fold geometries after depth conversion with the CVMH, with rates determined using mean ages.

SAR step	Measurement parameters
1 Beta irradiation	0 (Nat), 20, 6.4, 64, 200, 640, 0, 20 Gy in turn
2 Preheat 1	60s at 250°C
3 $IRSL_{50}$ 1	2.5s 90% laser power at 50°C
4 $IRSL_{225}$ 2	2.5s 90% laser power at 225°C
5 Beta test dose	9 Gy
6 Preheat 2	60s at 250°C
7 $IRSL_{50}$ S1 Sensitivity measurement	2.5s 90% laser power at 50°C
8 $IRSL_{225}$ S2 Sensitivity measurement	2.5s 90% laser power at 225°C
9 Hot bleach – then return to 1	40s IRSL (diodes at 90% power) at 290°C

Data Repository Table 2. Steps used in the post-IR IRSL single aliquot regenerative-dose (SAR) protocol applied to K-feldspar single grains. Multiple cycles of measurement were made to 200 to 400 grains for each sample.

Supplemental references

Allen, P. A. & Allen, J. R., 2005, Basin Analysis, Oxford, U.K., Blackwell Publishing.

Bahr, D. B., Hutton, E., Syvitski, J. & Pratson, L. F., 2001, Exponential approximations to compacted sediment porosity profiles: Computers & Geosciences, v. 27, p. 691–700.

Bassinot, F. C. et al., 1994, The Astronomical Theory of Climate and the Age of the Brunhes-Matuyama Magnetic Reversal: Earth and Planetary Science Letters, v. 126, p. 91–108.

Benesh, N. P., Plesch, A., Shaw, J. H. & Frost, E. K., 2007, Investigation of growth fault bend

folding using discrete element modeling: Implications for signatures of active folding

above blind thrust faults, Journal of Geophysical Research, v. 112, B03S04, p. 2156-

2202.

Buylaert, J.P., Murray, A.S., Thomsen, K.J., Jain, M., 2009, Testing the potential of an elevated

temperature IRSL signal from K-feldspar,Radiation Measurements, v. 44, p. 560-565.

Chen, Y.-G. et al., 2007, Coseismic fold scarps and their kinematic behavior in the 1999 Chi-

Chi earthquake Taiwan, Journal of Geophysical Research, v. 112, B03S04, p. 2156-

2202.

Ehman, K. D. & Edwards, B. D., 2014, Sequence Stratigraphic Framework of Upper Pliocene

to Holocene Deposits, Los Angeles Basin, California: Implications for Aquifer

Architecture: Society for Sedimentary Geology (SEPM), ISBN: 978-0-9842302-5-9.

Galbraith, R.F., Roberts, R.G., Laslett, G.M., Yoshida, H. & Olley, J.M. 1999, Optical dating of

single and multiple grains of quartz from Jinmium rock shelter, northern Australia.

Part I, experimental design and statistical models, Archaeometry, v. 41, p. 339–364.

Hubbard, J., J. H. Shaw, J.F. Dolan, T. L. Pratt, L. McAuliffe, and T. K. Rockwell, 2014,

Structure and seismic hazard of the Ventura Avenue anticline and Ventura fault,

California: Prospect for large, multi-segment ruptures in the Western Transverse

Ranges: Bulletin of the Seismological Society of America, v. 104/3, p. 1070–1087.

Leon, L. A., 2009, Paleoseismology of blind-thrust faults beneath Los Angeles, California:

Implications for the potential of system-wide earthquakes to occur in an active fold-

and-thrust belt: Ph.D. Dissertation, University of Southern California, DAI/B 70-07.

Mitchum, R. M., Vail, P. R. & Thompson, S., III., 1977, Seismic Stratigraphy and Global

Changes of Sea Level: Part 2. The Depositional Sequence as a Basic Unit for

Stratigraphic Analysis: Section 2. Application of Seismic Reflection Configuration to

Stratigraphic Interpretation, in AAPG Special Volumes M 26: Seismic Stratigraphy -

Applications to Hydrocarbon Exploration, Tulsa, OK, USA, American Association of

Petroleum Geologists., p. 53–62.

Neal, J. & Abreu, V., 2009, Sequence stratigraphy hierarchy and the accommodation

succession method: Geology, v. 37, p. 779–782.

Neumaier, A. & Schneider, T., 2001, Estimation of parameters and eigenmodes of

multivariate autoregressive models: ACM T Math Software, v. 27, p. 27–57.

Reimer, P. J. et al., 2013, Intcal13 and Marine13 Radiocarbon Age Calibration Curves 0-

50,000 Years Cal Bp: Radiocarbon, v. 55, p. 1869–1887.

Rockwell, T. K., E. A. Keller, and G. R. Dembroff, 1988, Quaternary rate of folding of the

Ventura Avenue anticline, western Transverse Ranges, southern California: Geological

Society of America Bulletin v. 100, p. 850–858.

Rhodes, E. J., 2015, Dating sediments using potassium feldspar single-grain IRSL: Initial

methodological considerations: Quaternary International, v. 362, p. 14–22.

Rhodes, E.J., Fanning, P.C. & Holdaway, S.J., 2010, Developments in optically stimulated

luminescence age control for geoarchaeological sediments and hearths in western

New South Wales, Australia, Quaternary Geochronology, v. 5, p. 348-352.

Schneider, T. & Neumaier, A., 2001, Algorithm 808: ARfit - A matlab package for the

estimation of parameters and eigenmodes of multivariate autoregressive models:

ACM T Math Software, v. 27, p. 58–65.

Sclater, J. G. & Christie, P., 1980, Continental Stretching - an Explanation of the Post-Mid-

Cretaceous Subsidence of the Central North-Sea Basin: Journal of Geophysical Research, v. 85, p. 3711–3739.

Suppe, J. Geometry and Kinematics of Fault-Bend Folding: American Journal of Science, v. 283, p. 684–721.

Törnqvist, T. E., Wallinga, J. & Busschers, F. S., 2003, Timing of the last sequence boundary in a fluvial setting near the highstand shoreline—Insights from optical dating: Geology, v. 31, p. 279–282.